

Impacts of building-height variability on turbulent coherent structures and pollutant dispersion: Large-eddy simulations

Jong-Won Kim ^a, Jong-Jin Baik ^{a,*}, Seung-Bu Park ^b, Beom-Soon Han ^c

^a School of Earth and Environmental Sciences, Seoul National University, Seoul, South Korea

^b School of Environmental Engineering, University of Seoul, Seoul, South Korea

^c Department of Environment and Energy, Semyung University, Jecheon, Chungcheongbuk-do, South Korea



ARTICLE INFO

Keywords:

Turbulent coherent structure
Pollutant dispersion
Air quality
Building-height variability
Large-eddy simulation

ABSTRACT

In built-up urban areas, there are numerous buildings of various shapes and heights, and their collective impacts on urban flow and air quality are of great concern. Here, we numerically examine the impacts of building-height variability on turbulent coherent structures above an array of square buildings and pollutant dispersion using a large-eddy simulation model. Three simulations are conducted: no building-height variability case ($\sigma/H = 0$, where σ is the standard deviation of building heights and H is the average building height), small building-height variability case ($\sigma/H = 0.25$), and large building-height variability case ($\sigma/H = 0.5$). In the latter two cases, buildings of two different heights are alternately arranged. Pollutants are released from street level. As the building-height variability increases, the average pedestrian-level pollutant concentration decreases and its spatial variability becomes large. The building-height variability greatly influences turbulence intensity and vertical turbulent momentum and pollutant fluxes. The streamwise-elongated low- and high-speed flow structures appear in all three cases, and they are wider in the spanwise direction when there is building-height variability. Strong turbulent fluctuations seem to affect the spanwise extension of the high- and low-speed flow structures. Quadrant analysis shows that stronger ejection and sweep events are more frequent with increasing building-height variability. The regions of ejection (sweep) well coincide with those of pollutant ejection (pollutant sweep). When there is building-height variability, the streaky structures that appear also in the fields of instantaneous vertical turbulent momentum flux are somewhat wider in the spanwise direction.

1. Introduction

Flow and pollutant dispersion in built-up urban areas are considerably influenced by underlying surface geometries. Flow in built-up urban areas is in essence turbulent flow. Turbulent flow is characterized by unsteady and random-like features, but recurring organized structures appear in it, which are known as turbulent coherent structures (TCSs) or turbulent organized structures. The appearance and characteristics of TCSs over cities or urban-like surfaces have been revealed through Doppler lidar observations (Yagi et al., 2017; Cheliotis et al., 2021), indoor and outdoor experiments (Takimoto et al., 2011), and numerical simulations (Kanda, 2006; Inagaki et al., 2012; Park et al., 2013; Yoshida and Takemi, 2021). Low-speed streaks are one of the most commonly observed coherent structures.

TCSs such as streaky patterns of low-momentum regions commonly

occur regardless of underlying surface geometries (Kanda, 2006; Fesquet et al., 2009; Takimoto et al., 2013; Yoshida and Takemi, 2021). The overall spatial patterns of TCSs appear to be similar, but their statistical characteristics for different surface geometries differ, to some extent, temporally and spatially. Takimoto et al. (2013) conducted wind tunnel experiments of turbulent flow over building arrays and quantified the streamwise length and spanwise width of turbulent structures using a two-point correlation method. They found that the lengths and aspect ratios (length/width) of large-scale turbulent structures are well correlated with the boundary-layer thickness and velocity gradient, while dependency on the boundary-layer thickness and velocity gradient is weak for small-scale turbulent structures. Using a large-eddy simulation (LES) model, Yoshida and Takemi (2021) showed that TCSs below the canopy height are more isotropic over an array of buildings of different heights than over an array of buildings of equal heights. They also

Peer review under responsibility of Turkish National Committee for Air Pollution Research and Control.

* Corresponding author. School of Earth and Environmental Sciences, Seoul National University, Seoul 08826, South Korea.

E-mail address: jjbaik@snu.ac.kr (J.-J. Baik).

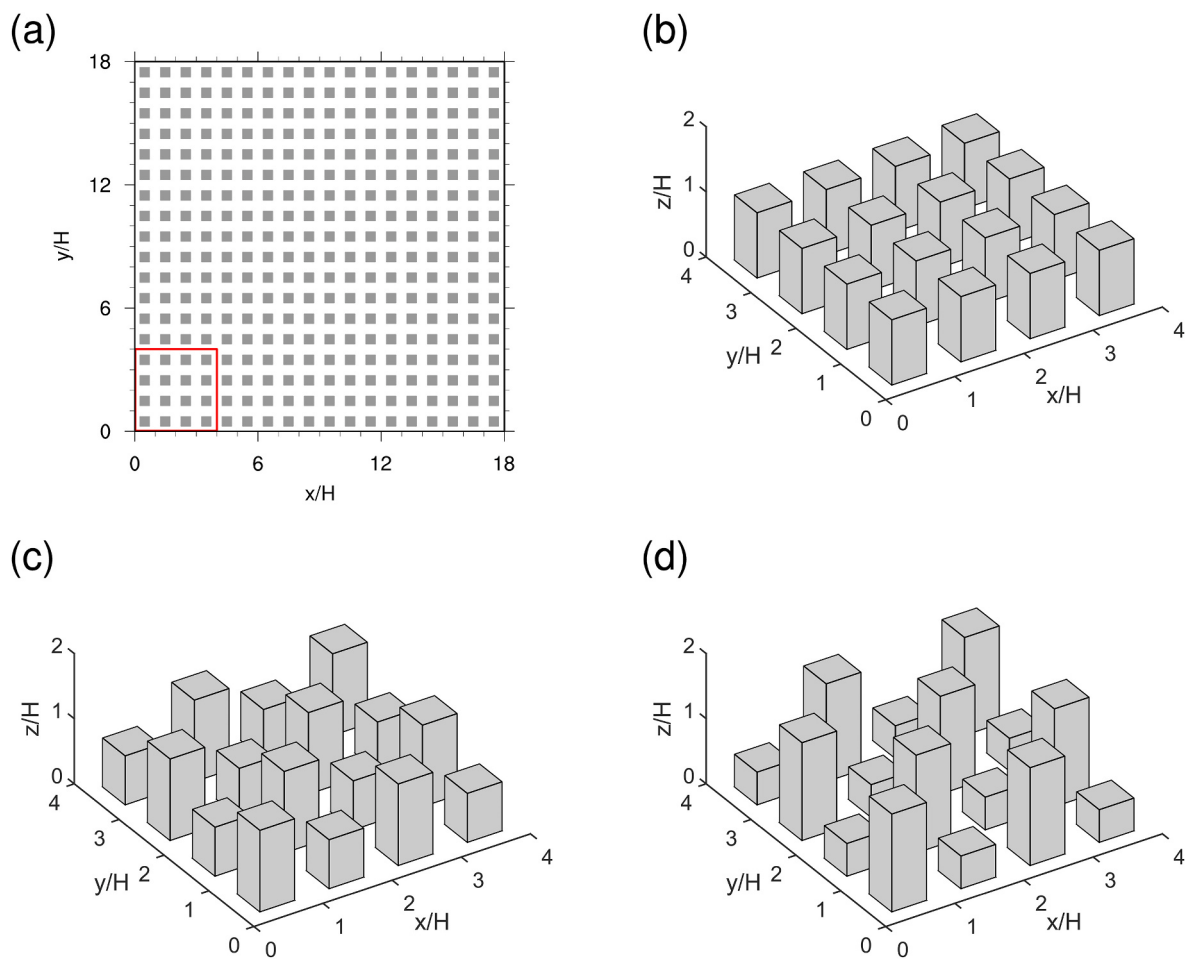


Fig. 1. Illustrations of (a) the plan view of computational domain and the three-dimensional building layouts (16 buildings included) in the (b) N-BHV, (c) S-BHV, and (d) L-BHV cases. The square in the red line in (a) indicates the horizontal area of the building layouts.

showed that at the heights of the roughness sublayer, the vertical inclination angles of ejection-centered turbulent structures are larger for larger building-height variability. These previous studies help to understand the impacts of urban surface geometries on the characteristics of TCSs.

In built-up urban areas, buildings of different heights greatly complicate flow therein. Xie et al. (2008) performed LESs of turbulent flow over urban-like geometries in which the heights of model buildings are randomly assigned. They showed that turbulence statistics within and immediately above the canopy are significantly different between the random-building-height simulation and uniform-building-height simulation. The Reynolds-averaged Navier-Stokes equation model simulations by Hang and Li (2010) indicate that the building height variation acts to enhance the vertical mean flow rate across the street-roof level, benefiting air ventilation in street canyons. Hamed et al. (2017) studied the impacts of obstacle-height heterogeneity on canopy turbulence using recirculating open channel equipment. They showed that uneven obstacle heights result in greater vertical turbulent exchange at the canopy interface. These studies emphasize the importance of building-height variability in enhancing vertical turbulent and mean exchange.

Dispersion of passive pollutants is controlled by the flow field. Thus, it is plausible that TCSs can play an important role in pollutant dispersion and the vertical turbulent pollutant flux is closely linked with the vertical turbulent momentum flux. However, few studies investigated the patterns and features of pollutant fluxes in association with TCSs over cities or urban-like surfaces. Park et al. (2013) examined turbulent pollutant dispersion over an array of cubical buildings using an LES

model and showed that pollutant ejection and pollutant sweep are related to streamwise-elongated low- and high-speed flow structures, respectively, and they mainly contribute to the vertical turbulent pollutant flux at the rooftop height. It would be interesting to investigate how the patterns and features of vertical turbulent pollutant flux in association with TCSs over an array of buildings differ with building-height variability.

In this study, we examine the impacts of building-height variability on TCSs and pollutant dispersion over urban-like surfaces. For this, we simulate turbulent flow and pollutant dispersion over an array of square buildings using an LES model. In section 2, the LES model and simulation design are described. In section 3, simulation results are presented and discussed. In section 4, a summary and conclusions are given.

2. Numerical model and simulation design

The numerical model used in this study is the parallelized LES model (PALM) (Maronga et al., 2020) version 6.0 which numerically solves filtered equations of velocity components, passive scalar concentration, and subgrid-scale turbulent kinetic energy (TKE) on a staggered Arakawa C-grid (Arakawa and Lamb, 1977). Note that the filter size in PALM is equal to the grid size in the simulation. The upwind-biased fifth-order difference scheme (Wicker and Skamarock, 2002) and the third-order Runge-Kutta difference scheme (Williamson, 1980) are used for spatial and temporal discretizations, respectively. A modified version of the 1.5-order Deardorff closure scheme (Deardorff, 1980) is used for the parameterization of subgrid-scale turbulent fluxes. PALM has been widely used for the simulations of turbulent flow and associated

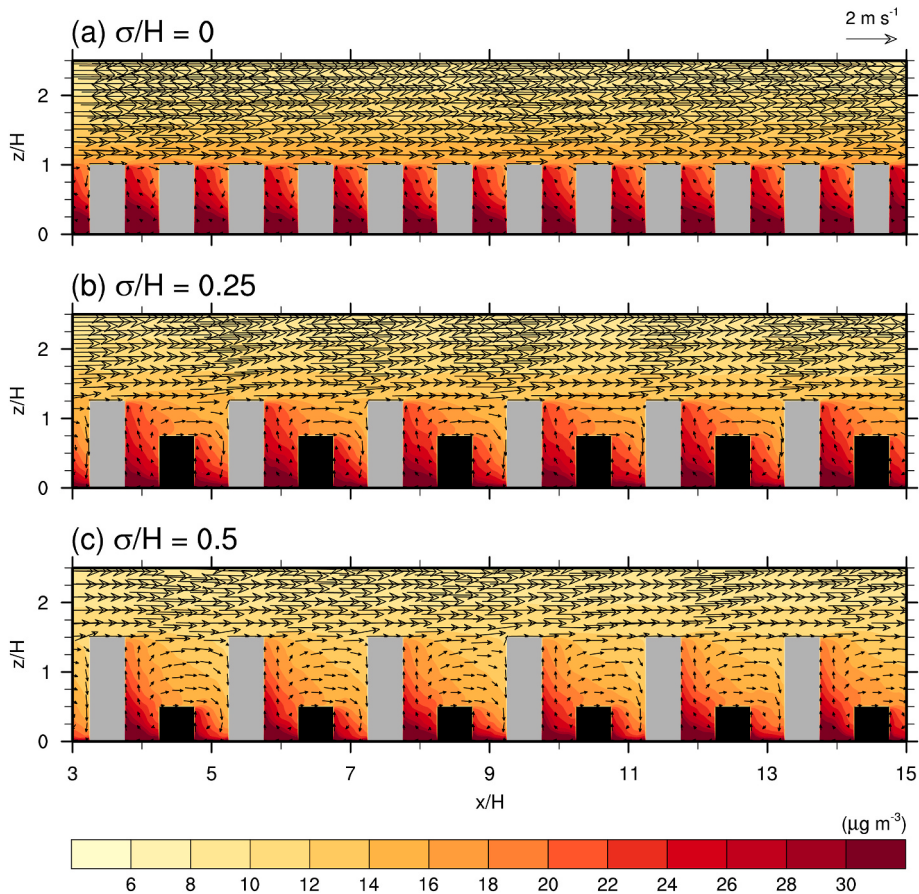


Fig. 2. Fields of temporally and spanwise averaged wind vector and pollutant concentration on the x - z plane in the (a) N-BHV, (b) S-BHV, and (c) L-BHV cases. The spanwise average considers 9 consecutive cross-section planes spaced at $2H$ intervals that pass the middle of buildings. In the S-BHV and L-BHV cases, the black and gray blocks indicate the short and tall buildings, respectively. In the N-BHV case, all buildings are indicated by the gray blocks.

pollutant dispersion over urban-like and urban geometries. It has been validated using wind tunnel data (Park et al., 2013; Razak et al., 2013; Han et al., 2018; Gronemeier et al., 2021). Park et al. (2013) performed a simulation with a rectangular building array considered in a wind tunnel experiment. They compared the two fields of the normalized mean pollutant concentration, one from PALM and the other from the wind tunnel experiment, and showed that the two fields are very similar to each other. Razak et al. (2013) performed PALM simulations with a staggered array of cubical blocks and compared the vertical profiles of the normalized mean streamwise velocity from PALM to those from the wind tunnel experiment. They found good agreement between the results, especially at heights below twice the block height.

In this study, the computational domain size is 1152 m in the x -direction (streamwise direction), 1152 m in the y -direction (spanwise direction), and 1260 m in the z -direction (vertical direction) with a grid number of 576 (x) \times 576 (y) \times 216 (z) (Fig. 1a). The grid size is 2 m both in the x - and y -directions. The grid size in the z -direction is 2 m up to $z = 160$ m, and above that level, it gradually increases with an expansion ratio of 1.08 until reaching the grid size 10 m. An array composed of square buildings with a side length of 32 m is considered. In the building array, a total of 324 (18 (x) \times 18 (y)) buildings are regularly aligned with a constant spacing of 32 m both in the x - and y -directions, with the plan area fraction of buildings 0.25. To examine the impacts of building-height variability on TCs and pollutant dispersion, three simulations with the same average building height of 64 m (H) but with different standard deviations of building heights ($\sigma = 0$, $0.25H$, and $0.5H$) are performed. The three cases are named as follows: N-BHV (no building-height variability; $\sigma/H = 0$), S-BHV (small building-height variability; $\sigma/H = 0.25$), and L-BHV (large building-height variability; $\sigma/H = 0.5$).

cases. In the N-BHV case, buildings with a height of H are regularly aligned in the domain (Fig. 1b). In the S-BHV and L-BHV cases, two types of buildings with heights of $H - \sigma$ and $H + \sigma$ are alternately arranged (Fig. 1c and d).

A uniform wind profile with a streamwise velocity of 5 m s^{-1} is initially imposed at the inflow boundary. The periodic boundary condition both in the x - and y -directions is applied for velocity components and pollutant concentration. At the top boundary, the zero-gradient boundary condition is applied. No-slip condition is applied at the building wall and bottom surface for velocity components. Passive pollutants are released from every grid point at the street bottom surface with a uniform pollutant flux of 1 $\mu\text{g m}^{-2} \text{s}^{-1}$, with reference to the magnitude of NO_x fluxes measured in Beijing, China (Squires et al., 2020). Coriolis force is not considered in this study. The LES model is integrated for 5400 s, and the simulation data for the last 900 s are used for analysis. Temporally and horizontally averaged flow and pollutant concentration are already in a quasi-steady state after 4500 s.

3. Results and discussion

3.1. Average flow and pollutant concentration

In this subsection, we examine how average flow and pollutant concentration differ with building-height variability. Fig. 2 shows the fields of temporally and spanwise averaged wind vector and pollutant concentration on the x - z plane in the N-BHV, S-BHV, and L-BHV cases. The time average is taken over the last 900 s. In the spanwise average, 9 consecutive cross-section planes spaced at $2H$ intervals that pass the middle of buildings are taken for the average. In all cases, the in-canyon

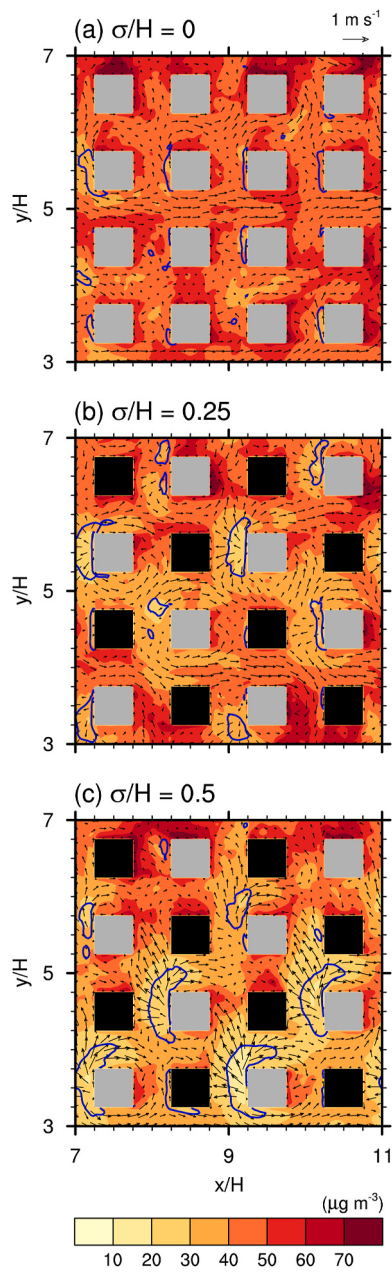


Fig. 3. Fields of temporally averaged wind vector and pollutant concentration on the x - y plane at $z/H = 0.03125$ in the (a) N-BHV, (b) S-BHV, and (c) L-BHV cases. In the S-BHV and L-BHV cases, the black and gray blocks indicate the short and tall buildings, respectively. In the N-BHV case, all buildings are indicated by the gray blocks. The blue contour lines indicate the vertical velocity of -0.03 m s^{-1} .

flow is mostly separated from the above-canyon flow. This type of flow is referred to as skimming flow (Oke, 1988). In the N-BHV case where building heights are equal, a clockwise vortex forms in the canyon and the pollutant concentration is higher near the leeward wall of a building (facing downstream) than near the windward wall of a building (facing upstream) (Fig. 2a). In the S-BHV and L-BHV cases where building heights are not equal, downdrafts near the windward wall of a tall building and updrafts near the leeward wall of a tall building appear (Fig. 2b and c), which have been reported in previous studies (Heist et al., 2009; Kim et al., 2022). In fact, updrafts are dominant in the canyon between a tall building and a short building behind it. The updrafts in front of the leeward wall of tall building transport near-street pollutants upward, producing high pollutant concentrations there. On

the other hand, the downdrafts near the windward wall of tall building transport relatively clean air downward, producing low pollutant concentrations there.

The fields of temporally averaged wind vector and pollutant concentration on the x - y plane at $z = 2 \text{ m}$ ($z/H = 0.03125$) in the three cases are presented in Fig. 3. The height $z = 2 \text{ m}$ is close to the pedestrian level where people are exposed to vehicle-emitted pollutants. In the N-BHV case, flows are generally weak in front of and behind a building and weak downdrafts often appear near the windward wall of a building. Overall, flows in the S-BHV and L-BHV cases are stronger and more complex than those in the N-BHV case. Relatively strong downdrafts in the S-BHV and L-BHV cases compared to the N-BHV case appear just in front of a tall building, which causes horizontally diverging flows. The relatively strong downdrafts and horizontally diverging flows are particularly pronounced in the L-BHV case. Due to the intrusion of relatively clean air by the downdrafts near the windward wall of a tall building, the pedestrian-level pollutant concentration is lower in the S-BHV and L-BHV cases than in the N-BHV case. The temporally and horizontally averaged pollutant concentrations at the pedestrian level are 51.4 , 41.7 , and $40.5 \mu\text{g m}^{-3}$ in the N-BHV, S-BHV, and L-BHV cases, respectively. The averaged pollutant concentrations in the S-BHV and L-BHV cases are 0.81 and 0.79 times that in the N-BHV case, respectively, indicating that pedestrian-level air pollution is reduced by about 20% when there is building-height variability. The improvement in air quality is much larger between the S-BHV and N-BHV cases (19%) than between the L-BHV and S-BHV cases (3%). Compared to the N-BHV case, the spatial variability of pedestrian-level pollutant concentration in the S-BHV and L-BHV cases is larger. The standard deviations of temporally averaged pollutant concentration are 9.0 , 11.2 , and $12.1 \mu\text{g m}^{-3}$ in the N-BHV, S-BHV, and L-BHV cases, respectively.

3.2. Vertical profiles of average flow, pollutant concentration, TKE, and turbulent fluxes

Next, we examine the vertical profiles of temporally and horizontally averaged streamwise velocity $\langle u \rangle$, pollutant concentration $\langle c \rangle$, TKE, vertical velocity variance $\langle w^2 \rangle$, vertical turbulent momentum flux, and vertical turbulent pollutant flux in the N-BHV, S-BHV, and L-BHV cases (Fig. 4). The vertical turbulent momentum flux and vertical turbulent pollutant flux are expressed by $\langle u'w' \rangle$ and $\langle c'w' \rangle$, respectively. Here, u , w , and c indicate the streamwise velocity, vertical velocity, and pollutant concentration, respectively. The angle bracket and overbar denote the horizontal average and temporal average, respectively, and the prime denotes the deviation from the horizontal average. Since the magnitudes of subgrid-scale (unresolved) parts are much smaller than those of grid-scale (resolved) parts (mostly by a factor of 10^{-2} or less), they are not included in the turbulence statistics of Fig. 4. The average streamwise velocity monotonically increases with height with its large increase across tall-building height in the S-BHV and L-BHV cases and the building height ($z/H = 1$) in the N-BHV case (Fig. 4a). The average streamwise velocity decreases with increasing building-height variability. Below $z/H \sim 1$, as the building-height variability increases, the average pollutant concentration decreases (Fig. 4b). Above $z/H \sim 1.25$, the three vertical profiles of the average pollutant concentration are almost the same.

The average TKE between $z/H \sim 0.25$ and $z/H \sim 1$ is smaller in the S-BHV and L-BHV cases than in the N-BHV case (Fig. 4c). Above $z/H \sim 1.5$, the average TKE increases with increasing building-height variability. Overall, the average vertical velocity variance increases with increasing building-height variability (Fig. 4d), implying that larger building-height variability leads to larger vertical velocity fluctuations. Local minimum peaks of the average vertical velocity variance appear at the heights of tall and short buildings in the S-BHV and L-BHV cases, and its local minimum peak appears at the building height in the N-BHV case. The average vertical turbulent momentum flux is negative (i.e.,

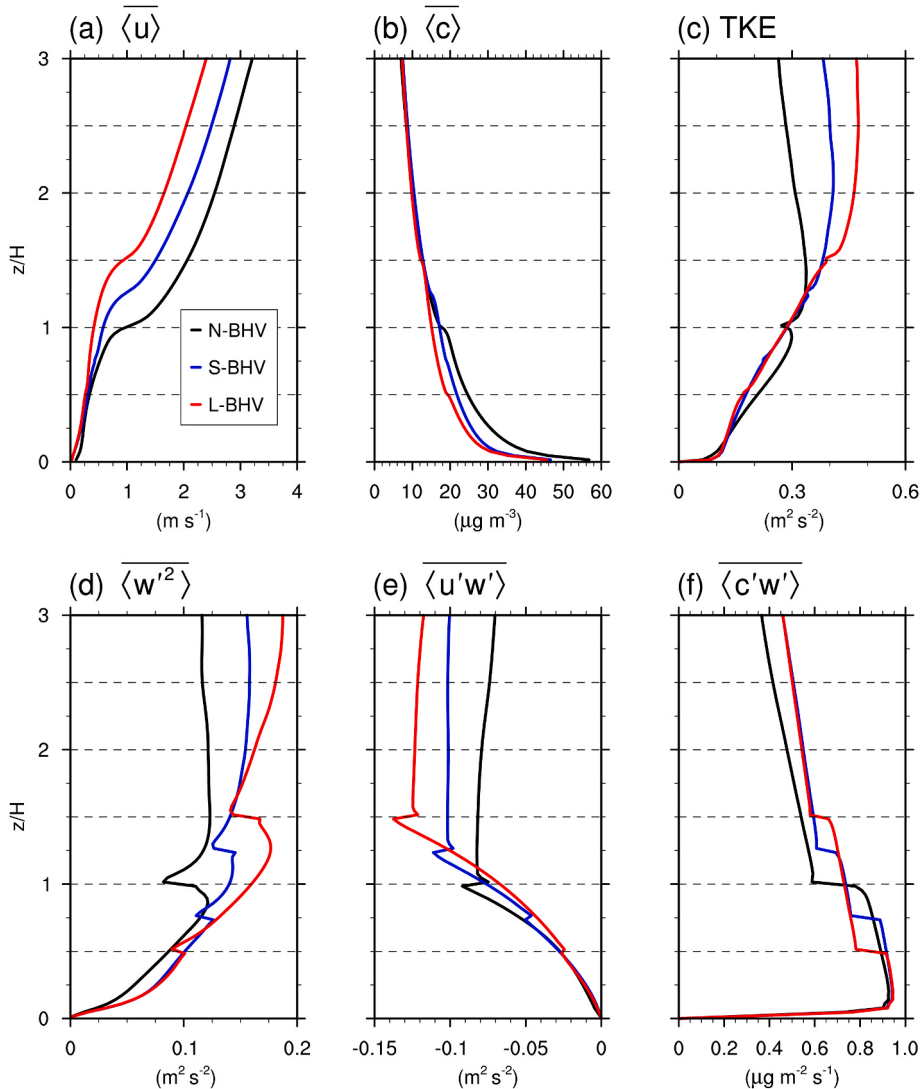


Fig. 4. Vertical profiles of temporally and horizontally averaged (a) streamwise velocity, (b) pollutant concentration, (c) turbulent kinetic energy, (d) vertical velocity variance, (e) vertical turbulent momentum flux, and (f) vertical turbulent pollutant flux in the N-BHV, S-BHV, and L-BHV cases.

downward) in all cases (Fig. 4e). The magnitude of the average vertical turbulent momentum flux is maximal at tall-building height in the S-BHV and L-BHV cases and the building height in the N-BHV case, and above $z/H \sim 1.25$, it increases with increasing building-height variability. The vertical profiles of the average vertical turbulent pollutant flux exhibit noticeable decreases at the heights of tall and short buildings in the S-BHV and L-BHV cases and the building height in the N-BHV case (Fig. 4f). Above $z/H \sim 1$, the average vertical turbulent pollutant flux is larger in the S-BHV and L-BHV cases than in the N-BHV case. Above $z/H \sim 1.5$, the difference in the average vertical turbulent pollutant flux between the S-BHV and L-BHV cases is negligible. Fig. 4c–f indicates that the building-height variability greatly influences turbulence intensity and vertical turbulent momentum and pollutant transports.

We also examined the vertical profiles above $z/H \sim 3$. Above $z/H \sim 3$, the average streamwise velocity monotonically increases with height and the average pollutant concentration, TKE, vertical velocity variance, vertical turbulent momentum flux (magnitude), and vertical turbulent pollutant flux monotonically decrease with height. At $z/H \sim 12$, the average streamwise velocity becomes 5 m s^{-1} (the initial value of streamwise velocity) and the average pollutant concentration, TKE, vertical velocity variance, vertical turbulent momentum flux, and vertical turbulent pollutant flux become 0.

3.3. Instantaneous flow and pollutant concentration, and coherent structures

To investigate the impacts of building-height variability on TCSs above a building array, the fields of u' on the $y-z$ plane at $x = 736 \text{ m}$ ($11.5H$) and $t = 5400 \text{ s}$ in the N-BHV, S-BHV, and L-BHV cases are presented in Fig. 5. The green contour lines are added to distinguish the regions of relatively high and low pollutant concentrations in association with TCSs. In all cases, high- and low-speed regions alternately appear in the spanwise direction. Relatively polluted air tends to be transported upward in low-speed regions, while relatively clean air tends to be transported downward in high-speed regions (see the $10 \mu\text{g m}^{-3}$ isolines). While not a novel deduction from our work (e.g., Park et al., 2013; Han et al., 2018), these features are worth noting in that they show that TCSs act both on the transports of pollutants and momentum. The spanwise widths of high- and low-speed regions are larger in the S-BHV and L-BHV cases than in the N-BHV case. It seems that strong turbulent fluctuations influence the spanwise extension of high- and low-speed regions. Note that the described characteristics of TCSs repeatedly appear in time.

Fig. 6 shows the fields of u' and c' on the $x-y$ plane at $z = 128 \text{ m}$ ($2H$) and $t = 5400 \text{ s}$ in the three cases. In the N-BHV case, streamwise-elongated high- and low-speed regions are seen (e.g., a high-speed

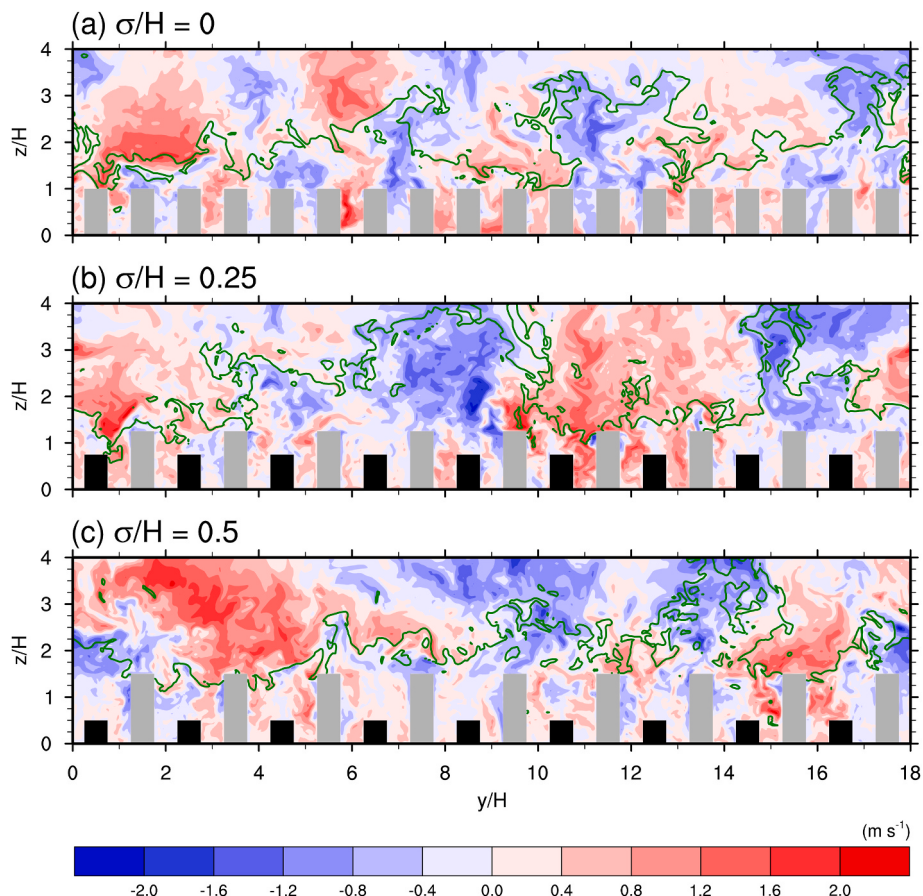


Fig. 5. Fields of u' on the $y-z$ plane at $x/H = 11.5$ and $t = 5400$ s in the (a) N-BHV, (b) S-BHV, and (c) L-BHV cases. In the S-BHV and L-BHV cases, the black and gray blocks indicate the short and tall buildings, respectively. In the N-BHV case, all buildings are indicated by the gray blocks. The green contour lines indicate the pollutant concentration of $10 \mu\text{g m}^{-3}$.

region at $y/H \sim 1-2$ and a low-speed region at $y/H \sim 16-17$ (Fig. 6a). In the S-BHV and L-BHV cases, some high- and low-speed regions are extended in the spanwise direction compared to the N-BHV case (Fig. 6c and e). The streaky structure seen in the N-BHV case is less pronounced and widened in the L-BHV case. The standard deviations of u' at $z = 128$ m are 0.58 , 0.65 , and 0.71 m s^{-1} in the N-BHV, S-BHV, and L-BHV cases, respectively. This implies that the spatial variability of streamwise velocity perturbation is larger with increasing building-height variability. The horizontal distribution of c' (Fig. 6b, d, and f) is well correlated with that of u' . The region of relatively high (low) pollutant concentration tends to coincide with the region of relatively low (high) streamwise velocity. This shows that the close relationship between the two variables is well represented not only in the $y-z$ plane (Fig. 5) but also in the $x-y$ plane. The correlation coefficient between u' and c' at $z = 128$ m over the last 900 s is -0.62 in the N-BHV case, -0.61 in the S-BHV case, and -0.65 in the L-BHV case. As in the $y-z$ plane, the described characteristics of TCSs appear repeatedly in the $x-y$ plane during the analysis time.

At the height of interest $z = 2H$, the temporally and horizontally averaged streamwise velocity is about 2.5 , 2.1 , and 1.6 m s^{-1} in the N-BHV, S-BHV, and L-BHV cases, respectively (Fig. 4). If the horizontal size of the domain is divided by the average streamwise velocity, the average time for a single turbulent coherent structure to pass through both ends of the domain can be calculated. The average time is 461 s in the N-BHV case, 549 s in the S-BHV case, and 720 s in the L-BHV case. Thus, the use of 900 s for analysis purposes in this study is appropriate since it is long enough for a single turbulent coherent structure passing over the entire domain.

To justify the choice of the computational domain size used in this

study, two simulations ($\sigma/H = 0$ and $\sigma/H = 0.5$) are performed in which the horizontal size of domain is halved ($9H \times 9H$) and the vertical domain size is kept the same (1260 m). For this domain size, high- and low-speed flow structures elongated in the streamwise direction are also evident but their spatial patterns are not sufficiently well revealed due to the small domain size. This indicates that a larger horizontal domain size is better to capture the spatial patterns of the high- and low-speed flow structures. It seems that the domain size used in this study is appropriate.

Figs. 4–6 point out significant impacts of building-height variability on turbulent quantities and turbulent flow above the height of the (tall) building. When there is building-height variability, stronger building-induced turbulent eddies are generated and these turbulent eddies make a contribution to above-building coherent structures. However, it is unclear in which pathways and to what extent the turbulent eddies affect above-building coherent structures with building-height variability. Novel analysis may be needed to answer this question, deserving future investigation.

Spectral analysis is performed to investigate the impacts of building-height variability on the spanwise extension of high- and low-speed regions (Fig. 7). Here, the power spectral density is first calculated using 576 grid-point data in the spanwise direction at every time and x/H and then the temporal and streamwise average is taken. Here, the temporal and streamwise average is performed in order to smoothen the sensitivity to streamwise location x and time. To focus on the y -direction spatial scale of turbulent coherent structures showing large spectral energies, we present the x -axis with wavelength rather than wavenumber. In the N-BHV case, the power spectral density peaks at a wavelength of 384 m which is one-third of the spanwise size of the

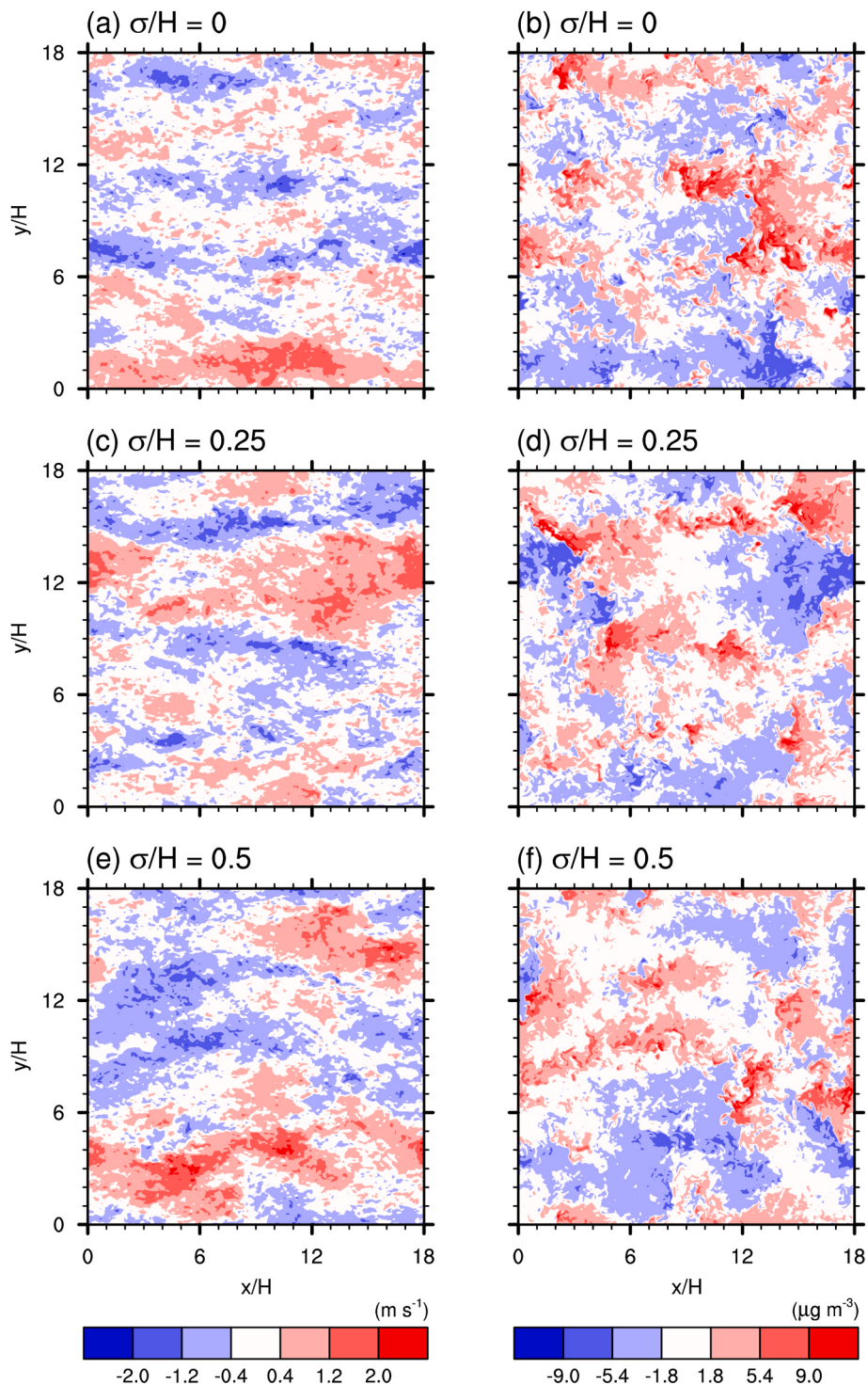


Fig. 6. Fields of u' (left column) and c' (right column) on the x - y plane at $z/H = 2$ and $t = 5400$ s in the (a, b) N-BHV (c, d) S-BHV, and (e, f) L-BHV cases.

computational domain. In the S-BHV case, the peak appears also at a wavelength of 384 m and the power spectral density at a wavelength of 576 m is close to that at the 384-m wavelength. The power spectral density in the L-BHV case monotonically increases with wavelength and exhibits no peak. The power spectral density at spanwise wavelengths larger than 384 m noticeably becomes larger with increasing building-height variability. This implies that larger building-height variability leads to more active turbulent structures at large scales in the spanwise direction.

To further investigate the impacts of building-height variability on

the intensity of turbulence, the probability density distributions of u' and c' at $z = 128$ m in the three cases are presented in Fig. 8. Note that data at all x , y , and t at this height are included in the calculation of the probability density distributions. As the building-height variability increases, the tails of the probability density distribution of u' extend (Fig. 8a). This means that the occurrence frequency of enhanced and widened high- and low-speed regions increases with increasing building-height variability. The probability density distributions of c' are almost the same in the three cases (Fig. 8b), which indicates that the probability density distributions of c' are not significantly affected by building-height

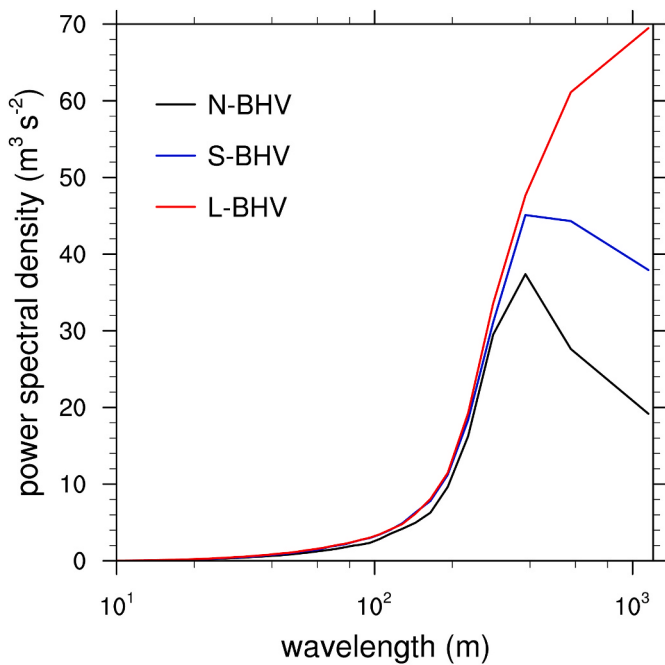


Fig. 7. Temporally and streamwise averaged power spectral densities of u' at $z/H = 2$ in the N-BHV, S-BHV, and L-BHV cases.

variability. It is interesting that unlike the spatial distributions of u' and c' which are closely related to each other (Fig. 6), the probability density distributions of u' and c' show different characteristics. These features need to be examined in more detail in a future study.

To examine the grid size dependency, an additional simulation with a grid size of 1 m is performed for the L-BHV case. In the additional simulation, the number of vertical grid is adjusted to 360 so that the vertical domain size is almost the same as that in the simulation with a grid size of 2 m. The temporally and streamwise averaged power spectral density at $z = 2H$ in the additional simulation shows features very similar to those in the simulation with a grid size of 2 m (Fig. 7) (not shown). This result suggests that the grid size does not significantly affect the spanwise distribution of TCSs and our resolution is sufficient.

3.4. Turbulent fluxes and coherent structures

In studies of turbulence, quadrant analysis is often used in which turbulent events are divided into four types according to the signs of

deviations of two variables. Quadrant analysis enables us to know how frequently a particular event occurs and how much the event contributes to the total turbulent fluxes (Raupach, 1981; Wallace, 2016). Quadrants for $u'w'$ are as follows: Q1: $u' > 0, w' > 0$ (outward interaction), Q2: $u' < 0, w' > 0$ (ejection), Q3: $u' < 0, w' < 0$ (inward interaction), and Q4: $u' > 0, w' < 0$ (sweep). Quadrants for $c'w'$ are as follows: Q1: $c' > 0, w' > 0$ (pollutant ejection), Q2: $c' < 0, w' > 0$ (pollutant outward interaction), Q3: $c' < 0, w' < 0$ (pollutant sweep), and Q4: $c' > 0, w' < 0$ (pollutant inward interaction).

Fig. 9 shows the fields of the joint probability densities of u' and w' and those of c' and w' at $z = 128$ m in the N-BHV, S-BHV, and L-BHV cases. The joint probability density of the two variables α and β is calculated using $f_{\alpha,\beta}(a_i, b_j) = P(a_i - 0.5\Delta\alpha < \alpha \leq a_i + 0.5\Delta\alpha, b_j - 0.5\Delta\beta < \beta \leq b_j + 0.5\Delta\beta)$. Here, a_i and b_j are the centers of α and β , respectively, and $\Delta\alpha$ and $\Delta\beta$ are the bin intervals of α and β , respectively (Han et al., 2018). The number of bins for u' , w' , and c' are uniformly 50. The bin intervals for u' , w' , and c' are 0.16 m s^{-1} , 0.16 m s^{-1} , and $0.64 \mu\text{g m}^{-3}$, respectively.

The joint probability density fields of u' and w' show that ejection and sweep are the two dominant events (Fig. 9a, c, and e). The dominance of the two events are natural because turbulent eddies tend to transport low-speed (high-speed) air parcel upward (downward) to reduce the vertical gradient of momentum. As the building-height variability increases, stronger ejection and sweep events are more frequent. For the $u'-w'$ subdomain of $-1.12 \text{ m s}^{-1} < u' \leq -0.80 \text{ m s}^{-1}$ and $0.32 \text{ m s}^{-1} < w' \leq 0.64 \text{ m s}^{-1}$, which corresponds to relatively strong ejection, the occurrence frequencies of the event are 1.7, 2.0, and 2.8% in the N-BHV, S-BHV, and L-BHV cases, respectively. For the whole $u'-w'$ domain, the occurrence frequency of ejection (sweep) is 0.31 (0.33) in the N-BHV case, 0.32 (0.32) in the S-BHV case, and 0.34 (0.32) in the L-BHV case. The ratio of the vertical turbulent momentum flux contributed by ejection (sweep) to the total vertical turbulent momentum flux is 0.73 (0.65) in the N-BHV case, 0.68 (0.69) in the S-BHV case, and 0.62 (0.69) in the L-BHV case. These results indicate that as the building-height variability increases, the occurrence frequency of ejection increases but the contribution of ejection to the total turbulent momentum flux decreases. The joint probability density fields of c' and w' show that the two dominant events are pollutant ejection and pollutant sweep (Fig. 9b, d, and f). The occurrence frequency of pollutant ejection (sweep) is 0.32 (0.35) in the N-BHV case, 0.32 (0.34) in the S-BHV case, and 0.34 (0.34) in the L-BHV case. The ratio of the vertical turbulent pollutant flux contributed by pollutant ejection (sweep) to the total vertical turbulent pollutant flux is 0.68 (0.57) in the N-BHV case, 0.65 (0.60) in the S-BHV case, and 0.62 (0.62) in the L-BHV case. The occurrence frequency of pollutant ejection does not

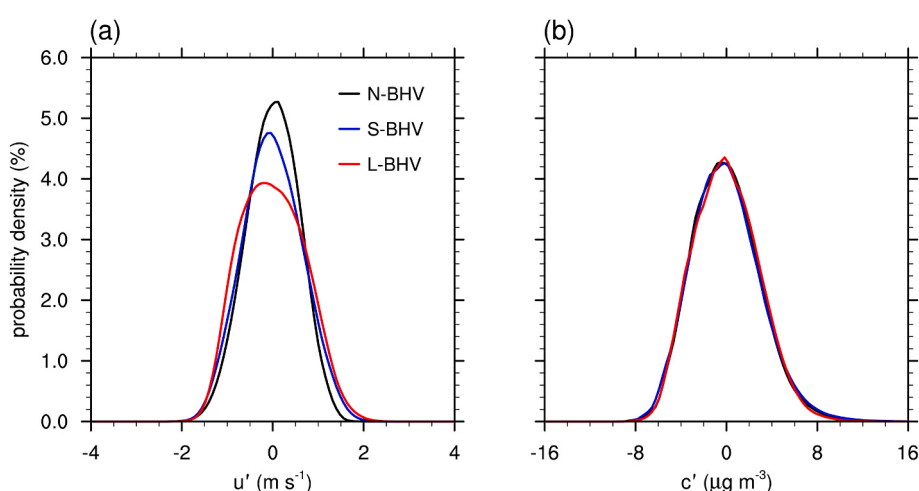


Fig. 8. Probability density distributions of (a) u' and (b) c' at $z/H = 2$ in the N-BHV, S-BHV, and L-BHV cases.

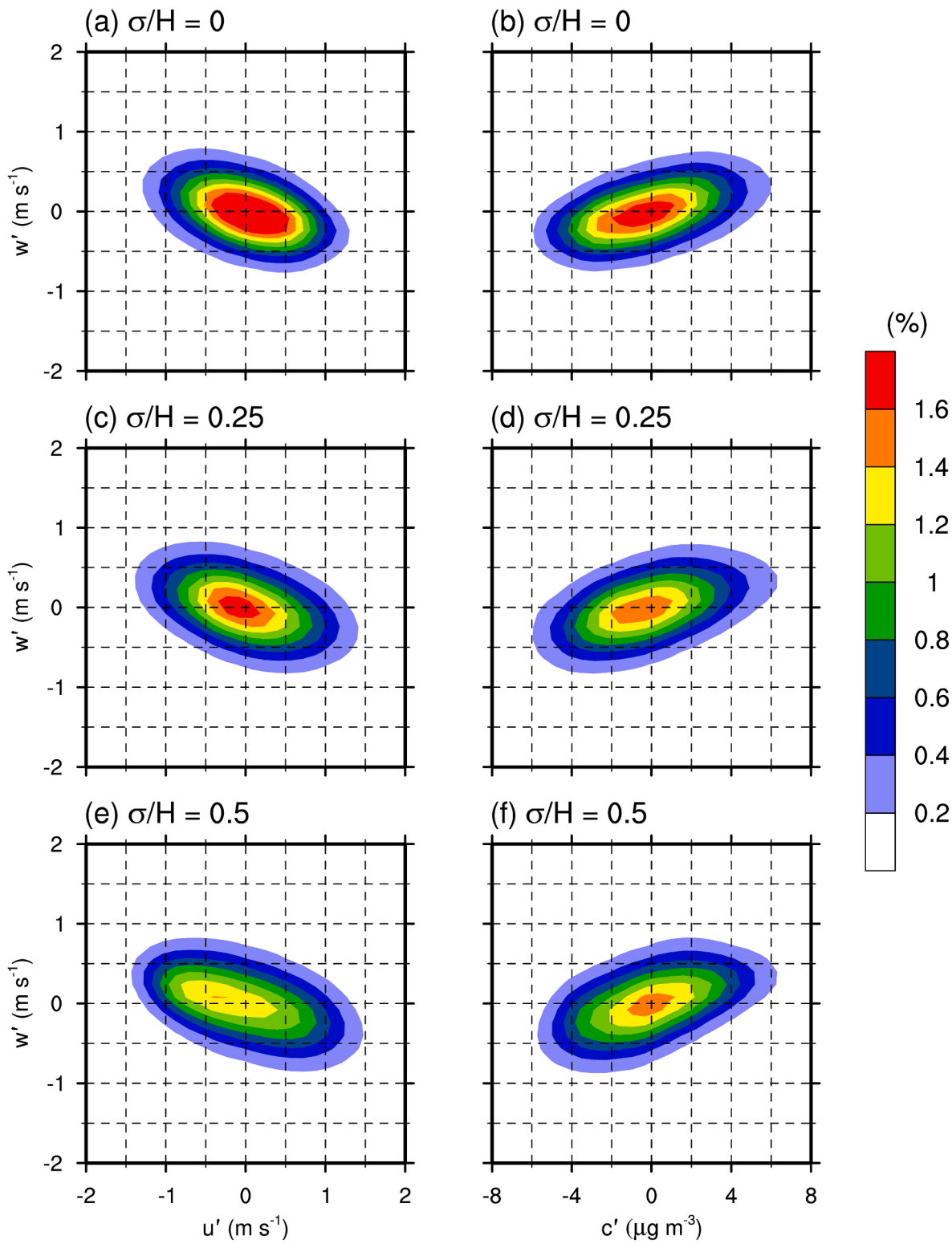


Fig. 9. Fields of the joint probability densities of u' and w' (left column) and c' and w' (right column) at $z/H = 2$ in the (a, b) N-BHV, (c, d) S-BHV, and (e, f) L-BHV cases.

change much with building-height variability. As in the joint probability densities of u' and w' , the contribution of pollutant ejection to the total turbulent pollutant flux decreases with increasing building-height variability. In each of the three cases, the occurrence frequency of ejection (sweep) is similar to that of pollutant ejection (sweep), indicating a close connection of pollutant ejection (sweep) with ejection (sweep).

Finally, we examine the impacts of building-height variability on the spatial distributions of dominant turbulent events and their association with high- and low-speed regions. For this, the fields of $\text{sgn}(w') \times \max(0, -u'w')$ and $\text{sgn}(w') \times \max(0, c'w')$ on the x - y plane at $z = 128 \text{ m}$ and $t = 5400 \text{ s}$ along with u' in the three cases are plotted (Fig. 10). Here, sgn denotes the sign function. The $\max(0, -u'w')$ and $\max(0, c'w')$ are non-zero only when the signs of $u'w'$ and $c'w'$ are negative and positive,

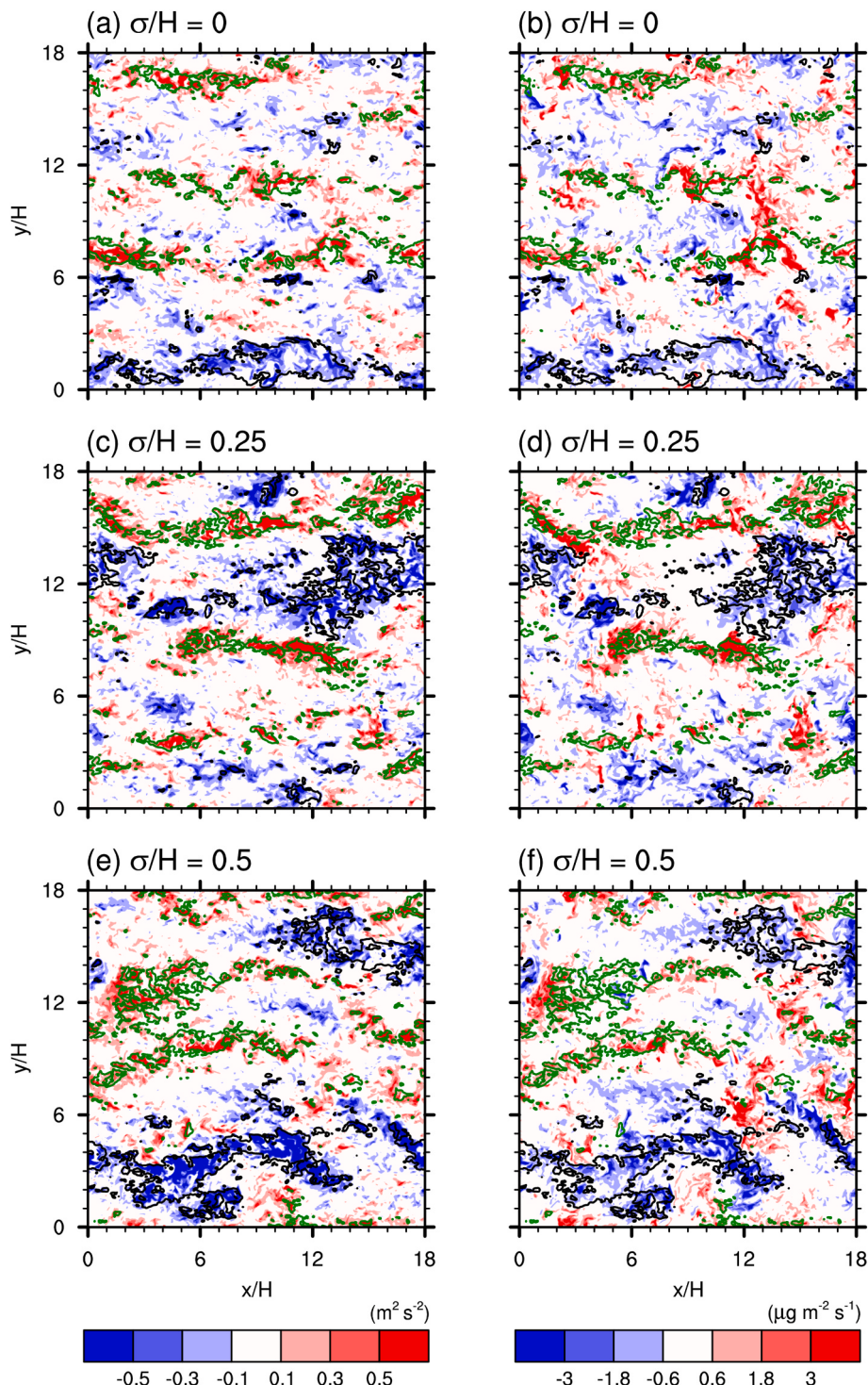


Fig. 10. Fields of $\text{sgn}(w') \times \max(0, -u'w')$ (left column) and $\text{sgn}(w') \times \max(0, c'w')$ (right column) on the x - y plane at $z/H = 2$ and $t = 5400 \text{ s}$ in the (a, b) N-BHV, (c, d) S-BHV, and (e, f) L-BHV cases. The black and green contour lines indicate u' of 1 m s^{-1} and -1 m s^{-1} , respectively.

respectively. Positive and negative values of $\text{sgn}(w') \times \max(0, -u'w')$ correspond to ejection and sweep, respectively, and positive and negative values of $\text{sgn}(w') \times \max(0, c'w')$ correspond to pollutant ejection and pollutant sweep, respectively (Park et al., 2013). u' isolines of 1 m s^{-1} and -1 m s^{-1} are selected to distinguish high- and low-speed regions in association with TCSs. In each of the N-BHV, S-BHV, and L-BHV cases, the spatial structures of ejection and sweep remarkably resemble those of pollutant ejection and pollutant sweep. The regions of ejection and sweep well coincide with the low-speed and high-speed regions,

respectively (Fig. 10a, c, and e). The regions of pollutant ejection and pollutant sweep well coincide with the low-speed and high-speed regions, respectively (Fig. 10b, d, and f). In the N-BHV case, streamwise-elongated strong ejection and sweep regions are evident (Fig. 10a). As in the instantaneous streamwise velocity perturbation (Fig. 6a, c, and e), the coherent structures revealed in the fields of instantaneous vertical turbulent momentum flux are wider in the spanwise direction in the S-BHV and L-BHV cases than in the N-BHV cases (Fig. 10a, c, and e). Strong turbulent fluctuations seem to be

responsible for this. The results from Figs. 5, 6 and 10 clearly show that high- and low-speed streaks are enhanced and widened by the building-height variability. Since there are strong interconnections among high- and low-speed streaks, turbulent events, and pollutant concentration, these results indicate the importance of building-height variability in atmospheric boundary-layer flow and air quality studies.

4. Summary and conclusions

In this study, we examined the impacts of building-height variability on turbulent coherent structures above an array of square buildings and pollutant dispersion. For this, three simulations are performed using a large-eddy simulation model: no, small, and large building-height variability cases. The average pedestrian-level pollutant concentration decreases with increasing building-height variability because strong vertical flows enhance pedestrian-level ventilation. In all three cases, the streamwise-elongated high- and low-speed flow structures are evident and the transports of momentum and pollutants by the high- and low-speed flow structures are closely related to each other. When there is building-height variability, they are wider in the spanwise direction probably because of stronger turbulent fluctuations. Quadrant analysis shows that as the building-height variability increases, stronger ejection and sweep events occur more frequently. The regions of ejection (sweep) well coincide with those of pollutant ejection (pollutant sweep). Although we found that the high- and low-speed flow structures tend to extend in the spanwise direction with increasing building-height variability, how turbulent eddies generated near buildings affect the high- and low-speed flow structures remains unclear. This deserves future investigation.

In built-up urban areas, there are numerous buildings of different heights which collectively affect turbulent flow therein (Park et al., 2015). It is practically as well as fluid-dynamically important to understand how spatial heterogeneity of building height in real urban areas influences the urban flow and air quality. This deserves future investigation, particularly focusing on turbulent coherent structures. In this study, thermal effects on flow and pollutant dispersion are not taken into consideration. It is well known that street bottom and/or building surface heating by incoming solar radiation greatly affect the urban flow and pollutant dispersion (e.g., Kim and Baik, 1999; Fatehi and Nilsson, 2022). As an extension of this study, it would be of interest to examine how the impacts of building-height variability on turbulent coherent structures and pollutant dispersion vary with street bottom and/or building surface heating.

Credit authorship statement

Jong-Won Kim: Formal analysis, Investigation, Data curation, Writing – original draft, Visualization. **Jong-Jin Baik:** Conceptualization, Formal analysis, Writing – original draft, Writing – review & editing, Supervision. **Seung-Bu Park:** Formal analysis, Investigation, Writing – review & editing. **Beom-Soon Han:** Formal analysis, Investigation, Writing – review & editing.

Declaration of competing interest

The authors declare that they have no known competing financial interests or personal relationships that could have appeared to influence the work reported in this paper.

References

- Arakawa, A., Lamb, V.R., 1977. Computational design of the basic dynamical processes of the UCLA general circulation model. *Methods Comput. Phys.* 17, 173–265.
- Cheliotis, I., Dieudonné, E., Delbarre, H., Sokolov, A., Dmitriev, E., Augustin, P., Fourmentin, M., Ravetta, F., Pelon, J., 2021. Properties of coherent structures over Paris: a study based on an automated classification method for Doppler lidar observations. *J. Appl. Meteorol. Climatol.* 60, 1545–1559.
- Deardorff, J.W., 1980. Stratocumulus-capped mixed layers derived from a three-dimensional model. *Boundary-Layer Meteorol.* 18, 495–527.
- Fatehi, H., Nilsson, E.J.K., 2022. Effect of buoyancy on dispersion of reactive pollutants in urban canyons. *Atmos. Pollut. Res.* 13, 101502.
- Fesquet, C., Drobinski, P., Barthlott, C., Dubos, T., 2009. Impact of terrain heterogeneity on near-surface turbulence structure. *Atmos. Res.* 94, 254–269.
- Gronemeier, T., Surm, K., Harms, F., Leitl, B., Maronga, B., Raasch, S., 2021. Evaluation of the dynamic core of the PALM model system 6.0 in a neutrally stratified urban environment: comparison between LES and wind-tunnel experiments. *Geosci. Model Dev.* 14, 3317–3333.
- Hamed, A.M., Sadowski, M.J., Nepf, H.M., Chamorro, L.P., 2017. Impact of height heterogeneity on canopy turbulence. *J. Fluid Mech.* 813, 1176–1196.
- Han, B.-S., Baik, J.-J., Kwak, K.-H., Park, S.-B., 2018. Large-eddy simulation of reactive pollutant exchange at the top of a street canyon. *Atmos. Environ.* 187, 381–389.
- Hang, J., Li, Y., 2010. Ventilation strategy and air change rates in idealized high-rise compact urban areas. *Build. Environ.* 45, 2754–2767.
- Heist, D.K., Brixey, L.A., Richmond-Bryant, J., Bowker, G.E., Perry, S.G., Wiener, R.W., 2009. The effect of a tall tower on flow and dispersion through a model urban neighborhood: part 1. Flow characteristics. *J. Environ. Monit.* 11, 2163–2170.
- Inagaki, A., Castillo, M.C.L., Yamashita, Y., Kanda, M., Takimoto, H., 2012. Large-eddy simulation of coherent flow structures within a cubical canopy. *Boundary-Layer Meteorol.* 142, 207–222.
- Kanda, M., 2006. Large-eddy simulations on the effects of surface geometry of building arrays on turbulent organized structures. *Boundary-Layer Meteorol.* 118, 151–168.
- Kim, J.-J., Baik, J.-J., 1999. A numerical study of thermal effects on flow and pollutant dispersion in urban street canyons. *J. Appl. Meteorol.* 38, 1249–1261.
- Kim, J.-W., Baik, J.-J., Han, B.-S., Lee, J., Jin, H.-G., Park, K., Yang, H., Park, S.-B., 2022. Tall-building effects on pedestrian-level flow and pollutant dispersion: large-eddy simulations. *Atmos. Pollut. Res.* 13, 101500.
- Maronga, B., Banzhaf, S., Burmeister, C., Esch, T., Forkel, R., Fröhlich, D., Fuka, V., Gehre, K.F., Geletić, J., Giersch, S., Gronemeier, T., Groß, G., Heldens, W., Hellsten, A., Hoffmann, F., Inagaki, A., Kadasch, E., Kanani-Sühring, F., Ketelsen, K., Khan, B.A., Knigge, C., Knoop, H., Krč, P., Kurppa, M., Maamari, H., Matzarakis, A., Mauder, M., Pallasch, M., Pavlik, D., Pfafferott, J., Resler, J., Rissmann, S., Russo, E., Salim, M., Schrempf, M., Schwenkel, J., Seckmeyer, G., Schubert, S., Sühring, M., von Tils, R., Vollmer, L., Ward, S., Witba, B., Wurps, H., Zeidler, J., Raasch, S., 2020. Overview of the PALM model system 6.0. *Geosci. Model Dev.* 13, 1335–1372.
- Oke, T.R., 1988. Street design and urban canopy layer climate. *Energy Build.* 11, 103–113.
- Park, S.-B., Baik, J.-J., Ryu, Y.-H., 2013. A large-eddy simulation study of bottom-heating effects on scalar dispersion in and above a cubical building array. *J. Appl. Meteorol. Climatol.* 52, 1738–1752.
- Park, S.-B., Baik, J.-J., Han, B.-S., 2015. Large-eddy simulation of turbulent flow in a densely built-up urban area. *Environ. Fluid Mech.* 15, 235–250.
- Raupach, M.R., 1981. Conditional statistics of Reynolds stress in rough-wall and smooth-wall turbulent boundary layers. *J. Fluid Mech.* 108, 363–382.
- Razak, A.A., Hagishima, A., Ikegaya, N., Tanimoto, J., 2013. Analysis of airflow over building arrays for assessment of urban wind environment. *Build. Environ.* 59, 56–65.
- Squires, F.A., Nemitz, E., Langford, B., Wild, O., Drysdale, W.S., Acton, W.J.F., Fu, P., Grinnmond, C.S.B., Hamilton, J.F., Hewitt, C.N., Hollaway, M., Kothaus, S., Lee, J., Metzger, S., Pingintha-Durden, N., Shaw, M., Vaughan, A.R., Wang, X., Wu, R., Zhang, Q., Zhang, Y., 2020. Measurements of traffic-dominated pollutant emissions in a Chinese megacity. *Atmos. Chem. Phys.* 20, 8737–8761.
- Takimoto, H., Sato, A., Barlow, J.F., Moriwaki, R., Inagaki, A., Onomura, S., Kanda, M., 2011. Particle image velocimetry measurements of turbulent flow within outdoor and indoor urban scale models and flushing motions in urban canopy layers. *Boundary-Layer Meteorol.* 140, 295–314.
- Takimoto, H., Inagaki, A., Kanda, M., Sato, A., Michioka, T., 2013. Length-scale similarity of turbulent organized structures over surfaces with different roughness types. *Boundary-Layer Meteorol.* 147, 217–236.
- Wallace, J.M., 2016. Quadrant analysis in turbulence research: history and evolution. *Annu. Rev. Fluid Mech.* 48, 131–158.
- Wicker, L.J., Skamarock, W.C., 2002. Time-splitting methods for elastic models using forward time schemes. *Mon. Weather Rev.* 130, 2088–2097.
- Williamson, J.H., 1980. Low-storage Runge-Kutta schemes. *J. Comput. Phys.* 35, 48–56.
- Xie, Z.-T., Coceal, O., Castro, I.P., 2008. Large-eddy simulation of flows over random urban-like obstacles. *Boundary-Layer Meteorol.* 129, 1–23.
- Yagi, A., Inagaki, A., Kanda, M., Fujiwara, C., Fujiyoshi, Y., 2017. Nature of streaky structures observed with a Doppler lidar. *Boundary-Layer Meteorol.* 163, 19–40.
- Yoshida, T., Takemi, T., 2021. Spatial characteristics of turbulent organized structures within the roughness sublayer over idealized urban surface with obstacle-height variability. *Environ. Fluid Mech.* 21, 129–154.